EXPERIMENTAL INVESTIGATION OF DEUTERON PHOTODISINTEGRATION IN THE Δ-RESONANCE REGION†

J. ARENDS, H.J. GASSEN, A. HEGERATH, B. MECKING, G. NÖLDEKE, P. PRENZEL, T. REICHELT and A. VOSWINKEL

Physikalisches Institut der Universität Bonn, Nussallee 12, 5300 Bonn, Federal Republic of Germany

and

W.W. SAPP

Laboratory for Nuclear Science, Massachusetts Institute of Technology, Cambridge, Massachusetts 02139, USA

Received 16 June 1983

Abstract: Differential cross sections for the deuteron photodisintegration process were measured for photon energies between 200 and 440 MeV using the tagged photon beam facility of the Bonn 500 MeV synchrotron. At eight angles between 18° and 145° charged particles were detected simultaneously in time-of-flight spectrometers consisting of scintillation counters. Above the resonance region the measured cross sections agree fairly well with earlier results, whereas there are larger discrepancies at low photon energies.

1. Introduction

The photodisintegration of the deuteron is one of the most fundamental processes in photonuclear physics. Therefore, careful experimental investigations and a detailed theoretical understanding of this process are of great importance for the whole field of photonuclear physics. At low photon energies the process is especially suited for the study of the deuteron wave function and details of the NN interaction. At higher photon energies, especially above the pion production threshold and in the region of the nucleon resonances, phenomena that go beyond the realm of classical nuclear physics, such as meson-exchange currents and isobar configurations, can be studied.

There is no satisfying theoretical treatment of the reaction in the region of the nucleon resonances. Early approaches [1-3]) were able to describe qualitatively the general features of the cross section in this energy range. In particular, the peak in the total cross section observed around 260 MeV excitation energy was explained as a consequence of Δ-creation followed by subsequent ΔN interaction. Recently,

more sophisticated theoretical calculations [4-7]) have been carried out. All calculations evaluate essentially the same diagrams. Differences occur for example in the treatment of the off-shell behavior of the pion photoproduction amplitude and in the description of the πNN vertex.

Deuteron photodisintegration above the pion production threshold has been investigated experimentally ever since high energy accelerators became available. The situation is very unsatisfactory: even if one considers only the seven most recent experiments [8-14]), discrepancies up to 50% are found in the data. Presumably, this confusing situation will only change if measurements performed at different laboratories will give the same results. Experiments to study the deuteron photodisintegration process are presently going on at Frascati and at MIT.

In the previous measurements different experimental techniques have been applied. However, all experiments [except ref. [14]] have been performed using a conventional bremsstrahlung beam. The photon energy had to be calculated from the measured kinematic quantities of the hadronic final state (normally the momentum of the outgoing proton). The photon flux in the accepted photon energy interval was determined usually by combining the total power in the beam (measured with a quantameter) and the (calculated or measured) shape of the photon energy spectrum. Thus, in addition to the uncertainties in each step of the procedure, there is a correlation between the determination of the proton energy and the photon flux. This kind of correlation is typical for wide-band neutral particle beams.

Though a monochromatic photon beam is not necessary for the measurement of a two-body reaction it obviously offers important advantages. Therefore, we have applied the tagged photon beam technique which also avoids the complicated normalization procedure common to the earlier measurements. The photon energy is determined by the energy difference between the initial and the final electron. The flux normalization is given directly by the counting rates of the tagging counters. In addition, the reaction is kinematically overdetermined (one-constraint fit) if the proton momentum is also measured. Protons from competing processes can be studied and can be easily separated.

2. Experimental setup

The experimental arrangement at the Bonn 500 MeV synchrotron is shown in fig. 1. The tagged bremsstrahlung beam [described in detail in ref. [15])] is produced by the circulating electron beam hitting a thin internal radiator situated near the end of the synchrotron magnet 5. The field of this magnet is used to momentum analyze electrons from the bremsstrahlung process. They are then detected in a hodoscope consisting of 24 scintillation counters. The photon energy range $k = (0.45-0.85)E_0$ (E_0 is the energy of the primary electrons) is covered simultaneously with an energy resolution of 10 MeV. For this experiment the mean intensity of the tagged beam was limited to about 10^5 photons/sec (at a duty factor of 3%) to
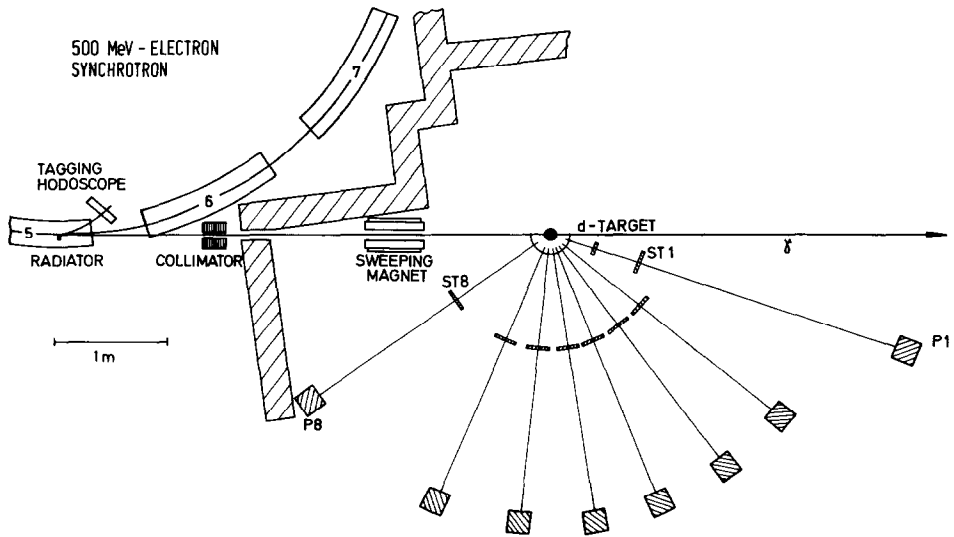
Fig. 1. Schematic view of the experimental setup. Details are explained in the text.

keep the contribution of random coincidences below 10%. The photon beam was collimated to a diameter of 5 cm at the target position. The photon definition probability P_γ, which is normally up to 0.98 in the uncollimated beam, was thereby reduced to 0.90.

After collimation the photon beam passed through a sweeping magnet and hit the target cell, a 9.0 cm diameter vertical cylinder filled with liquid deuterium at a pressure of 800 Torr; the kapton walls of the target cell were 125 µm thick.

Outgoing charged particles were detected simultaneously in eight time-of-flight spectrometers SP1–SP8 surrounding the target. The spectrometers were equally spaced in $\cos \theta_p^*$ between +0.9 and −0.9 (θ_p^* is the angle of the proton in the center-of-mass system). They consisted of the thin start counters ST1–ST8 (thickness $t = 1.0$ cm for ST1–ST4, $t = 0.5$ cm for ST5–ST8) and thick rear stop counters P1–P8 ($t = 20$ cm).

The P-counters, with a sensitive area of 20×100 cm^2, were set up vertically to restrict the acceptance in θ_p^* to ±3°. The solid angle of the spectrometers was determined primarily by the front area of the P-counters and their distances from the target (250 cm for SP2–SP8). The corresponding geometrical solid angle of 32 msr for each of the spectrometers had to be corrected for edge effects as described in sect. 3.

The most forward time-of-flight spectrometer SP1 was equipped with two start counters, and the associated P1 counter was set at a larger distance (320 cm). In both SP1 and SP2 the large number of electron and positron events from electromagnetic processes was reduced by requiring large pulse heights in the corresponding

start counters. This requirement also decreased the detection efficiency for high energy pions.

A trigger was defined by coincident signals from one of the time-of-flight arms and one of the tagging counters $(\sum SP_i) \times (\sum TC_i)$. All pulse heights and time differences were digitized by standard CAMAC modules. All data including the counting rates and the coincidence pattern were read via CAMAC by an on-line computer. The computer provided on-line data processing and graphic displays which considerably facilitated the supervision of the experiment.

To cover a wider photon energy range and to check the consistency of the data, measurements were performed at three different endpoint energies of the synchrotron (480, 455 and 440 MeV). The photon definition probability P_γ was measured regularly at reduced beam intensity ($\approx 10^3$ photons/sec) by putting a lead-glass Čerenkov counter directly in the photon beam.

3. Data analysis and corrections

The mass of charged particles was determined by combining the time-of-flight (target–P-counter) with the energy deposited in the P-counter. The particle identification capability of the system is demonstrated in fig. 2. Electrons and pions populate the region of short time of flight and small energy deposition; protons dominate the region of long time of flight. The Λ-shaped structure for the proton events arises because the thickness of the rear P-counter is just sufficient to stop 175 MeV protons. For protons with $T \leqslant 175$ MeV the P-counter acts as a total absorption counter, for $T > 175$ MeV as an energy loss detector.

After particle identification the momentum of charged pions and protons was calculated from the measured time of flight. For the proton events the photodisintegration process was separated from pion production by using the kinematical overdetermination. For each event the missing mass m_X was calculated from the known four-momenta of photon, deuteron and proton: $m_X^2 = p_X^2 = (p_\gamma + p_d - p_p)^2$. For the deuteron photodisintegration process m_X should be distributed around the neutron mass $m_X \approx m_n$, whereas $m_X \gtrsim m_n + m_\pi$ for events from pion photoproduction. As an example fig. 3 shows the measured m_X spectrum for protons registered in the most forward time-of-flight spectrometer SP1. The width of the peak around 940 MeV reflects the overall energy resolution of the apparatus. Recoil protons from pion production reactions produce the large bump for $m_X \geqslant 1080$ MeV. The cut-off at high missing mass is determined by the photon energy and the threshold for proton detection ($T_p^{min} = 50$ MeV).

Events in the unphysical regions $m_X < m_n$ and $m_\pi < m_X < m_n + m_\pi$ are due to protons produced in the target walls and to accidental coincidences between the time-of-flight arms and the tagging counters. The following background subtraction procedure was chosen in order to minimize the statistical fluctuations. The m_X distribution was fitted in the range $820 \leqslant m_X \leqslant 1060$ MeV to a gaussian peak on top
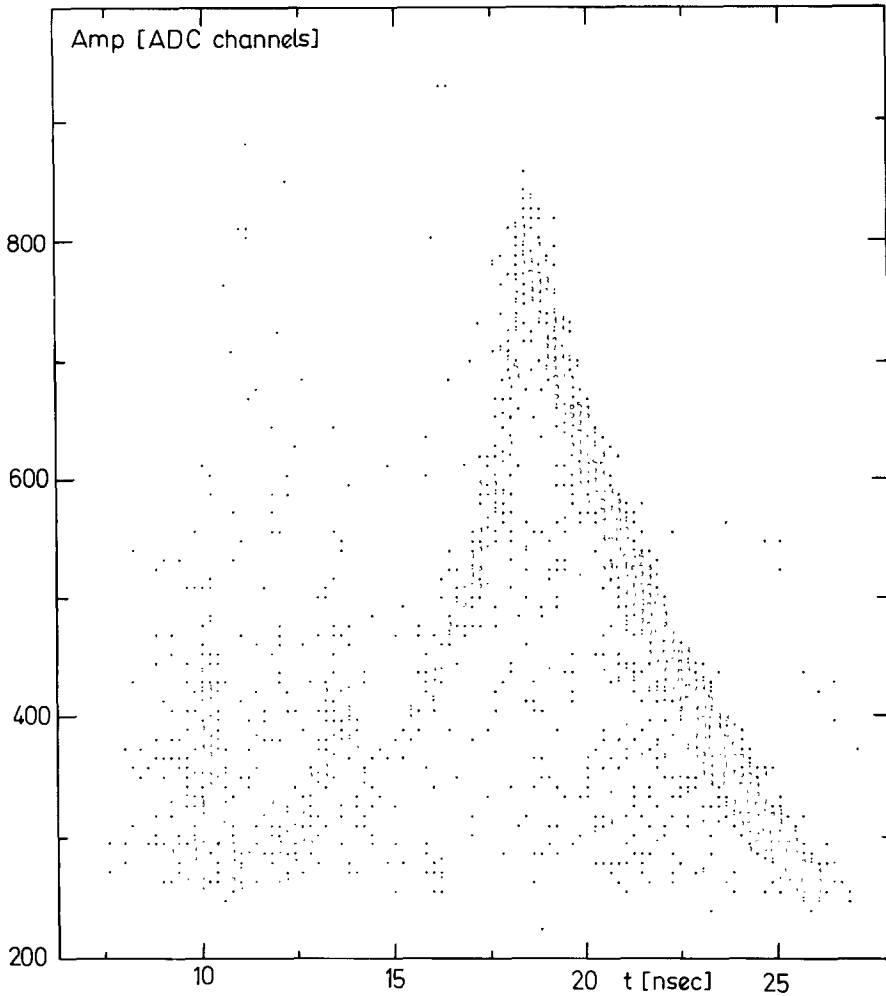
Fig. 2. Pulse height versus time of flight for the spectrometer SP1 ($\theta_p^{lab} = 18°$). The events are due to photons in the whole tagged energy range.

of a background. A function linear in the missing mass and quadratic in the photon energy was used to describe the background. The number of events from the photodisintegration process was then determined by subtracting the smoothed background from the experimental data. The integration over the missing mass peak was performed within the limits $m_X - 3\sigma$ and $m_X + 3\sigma$ where σ is the rms width of the gaussian line. This procedure takes care of accidental coincidences and protons from the target walls. It also eliminates protons that are emitted in secondary reactions of charged pions in the target itself or in the surrounding material. The background contribution is both energy and angle dependent; it amounts to 16%
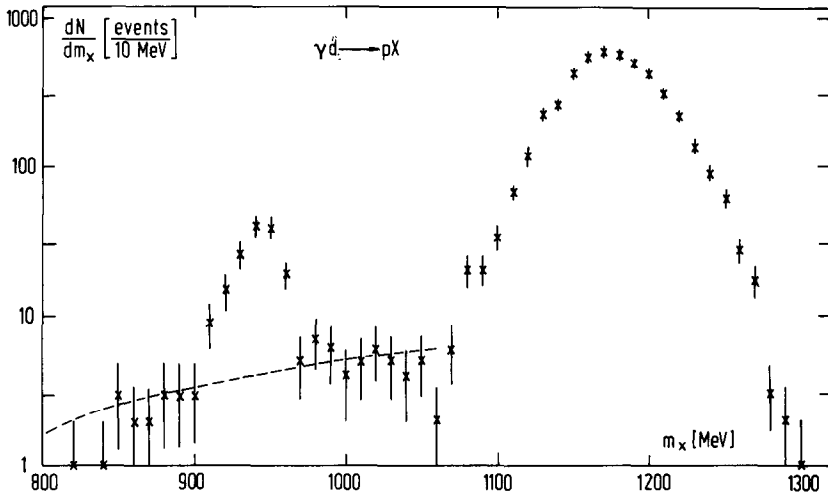
Fig. 3. Missing mass distribution for proton events in the time-of-flight spectrometer SP1. The events are due to tagged photons with $k = 400$ MeV. The dashed line gives the fit result for the background contribution. The data were collected during a run of duration 3 weeks. (Note the logarithmic scale.)

at $k = 200$ MeV, reaches a minimum of 10% at $k = 300$ MeV and increases to 22% at $k = 400$ MeV (in the time-of-flight spectrometer SP4).

A further correction had to be applied for protons that suffered multiple scattering or nuclear interaction before depositing enough energy in the P-counter. The resulting decrease of the effective solid angle was calculated by a Monte Carlo computer program taking the geometry of the setup and the cross section for nuclear interaction [16]) into account. The correction depends on the proton angle and the photon energy; in SP4 for example it amounts to 7% at $k = 200$ MeV increasing to 11% at $k = 400$ MeV. The corrections and the corresponding uncertainties for $d\sigma\,(\gamma d \rightarrow pn)/d\Omega$ are listed in table 1. The total systematic error for the photo-disintegration cross sections is estimated to be ±4%.

In addition to the effects mentioned above the pion data had to be corrected for the loss of events due to pion decay and for pions below the detection threshold. A further problem (not present in the proton data) is due to subnanosecond changes of the tagging counter timing signal which make the clean separation of electrons and pions difficult. Therefore, the uncertainties for the pion data are larger than for the proton data. The systematic error for $\sigma_{tot}(\gamma d \rightarrow \pi^{\pm} X)$ is estimated to be ±7%.

4. Results and discussion

The consistency and reproducibility of the experimental results were checked by measuring simultaneously with high statistical accuracy the cross sections for charged pion photoproduction. Since the pion detection efficiency in SP1 and SP2 was low

TABLE 1

Contributions to the total systematic error for the $\gamma d \to pn$ measurements

Error source	Systematic error
photon flux normalization	$\pm 1\%$
target thickness $\times$ density	$\pm 1\%$
spectrometer solid angle	$\pm 2\%$
nuclear interaction and multiple scattering	$\pm 2\%$
background subtraction	$\pm 2\%$
total	$\pm 4\%$

the total cross section had to be obtained from a fit to the differential cross sections using SP3–SP8 only. The results displayed in fig. 4 show the excellent long term stability of the setup. For comparison the total cross section for $\gamma d \to \pi^{\pm} X$ was synthesized from published results for the exclusive channels. For the $\gamma d \to \pi^{-} pp$
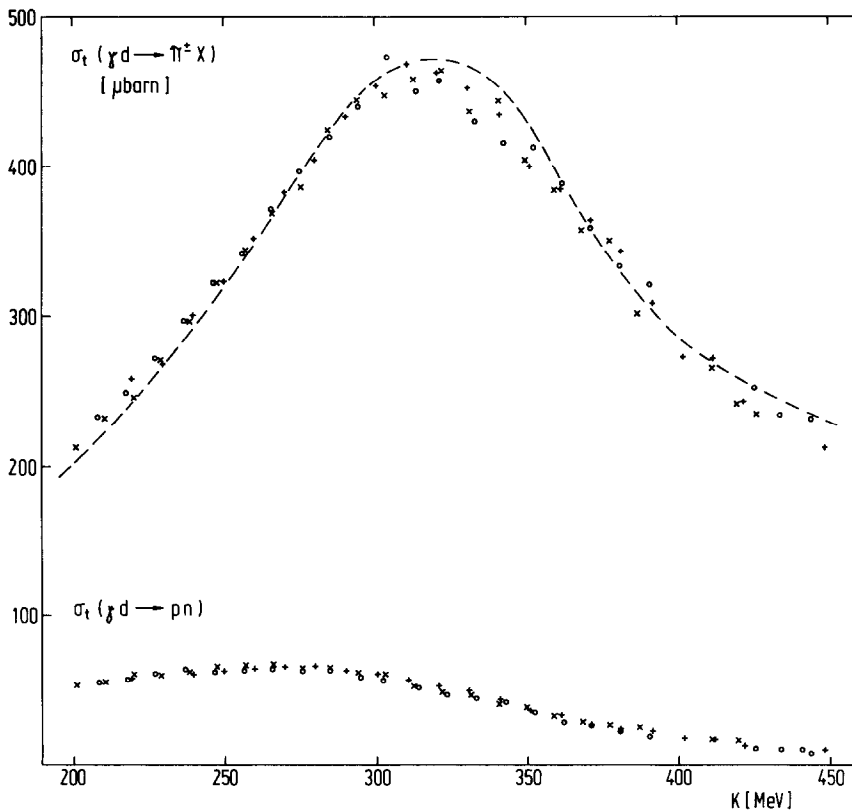

Fig. 4. Total cross section for charged pion photoproduction and deuteron photodisintegration as a function of the photon energy k. The results of the three runs at different endpoint energies are shown separately for $k = 480$ MeV $(+)$, 455 MeV $(\bigcirc)$ and 440 MeV $(\times)$. The dashed curve gives the synthesized cross section for $\gamma d \to \pi^{\pm} X$.

TABLE 2

Measured c.m.s. differential cross sections for $\gamma d \to pn$ in $\mu b/sr$

k (MeV)	SP1 $\theta_p^{lab}=18.7°$ $\theta_p^*=24.3°$	SP2 $38.6°$ $49.4°$	SP3 $53.6°$ $67.4°$	SP4 $68.0°$ $83.8°$	SP5 $81.6°$ $98.3°$	SP6 $96.4°$ $113.0°$	SP7 $116.3°$ $131.1°$	SP8 $145.4°$ $154.6°$
200	4.19±0.16	4.83±0.15	4.66±0.14	5.05±0.16	5.05±0.17	4.39±0.16	3.35±0.15	2.71±0.16
220	4.47±0.11	5.02±0.10	5.38±0.11	5.42±0.12	5.06±0.12	4.69±0.12	4.06±0.12	2.94±0.11
240	4.96±0.10	5.52±0.09	5.69±0.09	5.63±0.10	5.33±0.10	5.14±0.11	4.14±0.10	3.41±0.11
260	5.67±0.12	5.61±0.10	5.82±0.11	5.77±0.11	5.52±0.12	5.15±0.12	4.44±0.12	3.84±0.13
280	5.10±0.12	5.67±0.11	5.85±0.11	5.83±0.12	5.51±0.12	4.93±0.12	4.50±0.12	3.80±0.13
300	4.73±0.12	5.15±0.11	5.25±0.11	5.58±0.12	5.29±0.12	4.49±0.12	4.20±0.13	3.41±0.13
320	4.39±0.12	4.34±0.11	4.60±0.11	4.76±0.12	4.41±0.12	3.89±0.12	3.64±0.13	3.07±0.13
340	3.74±0.11	3.63±0.10	4.22±0.10	4.41±0.11	3.82±0.11	3.20±0.11	3.13±0.12	2.54±0.12
360	2.75±0.09	2.81±0.08	3.09±0.08	3.25±0.09	3.06±0.09	2.53±0.09	2.19±0.09	2.01±0.10
380	2.19±0.10	2.11±0.08	2.33±0.08	2.45±0.09	2.24±0.09	1.90±0.09	1.65±0.09	1.62±0.11
400	1.94±0.13	1.50±0.10	1.85±0.11	2.14±0.12	1.65±0.11	1.44±0.12	1.31±0.12	1.05±0.13
420	1.28±0.09	1.34±0.07	1.47±0.07	1.62±0.08	1.37±0.08	1.11±0.08	0.95±0.08	0.83±0.09
440	1.10±0.12	0.84±0.10	1.00±0.09	1.40±0.12	1.05±0.11	0.81±0.11	0.74±0.11	0.66±0.13

Only the statistical errors are quoted.

process the experimental results of Benz *et al.* [17]) were used. The total cross section for the $\gamma d \to \pi^+ nn$ reaction was derived from the experimental data for $\gamma p \to \pi^+ n$ [ref. [18])] multiplied by a correction factor [taken again from ref. [17])] to account for deuteron effects. The agreement between our results and the synthesized total cross sections is good.

For the deuteron photodisintegration process the results of the three runs were sorted into 20 MeV wide photon energy bins and then added to form one data set. The resulting differential cross sections are given in table 2; angular distributions are displayed in fig. 5. Our data at $k = 220$, 300 and 400 MeV are compared in fig. 6 with experimental results published since 1967 and with recent theoretical calculations. At 220 MeV there is excellent agreement among our data, the results of Anderson *et al.* [11]) and the prediction by Laget [4])[†]. The data of Buon *et al.* [10]) are about 15% lower but still show the same shape, while the results of Kose *et al.* [8])

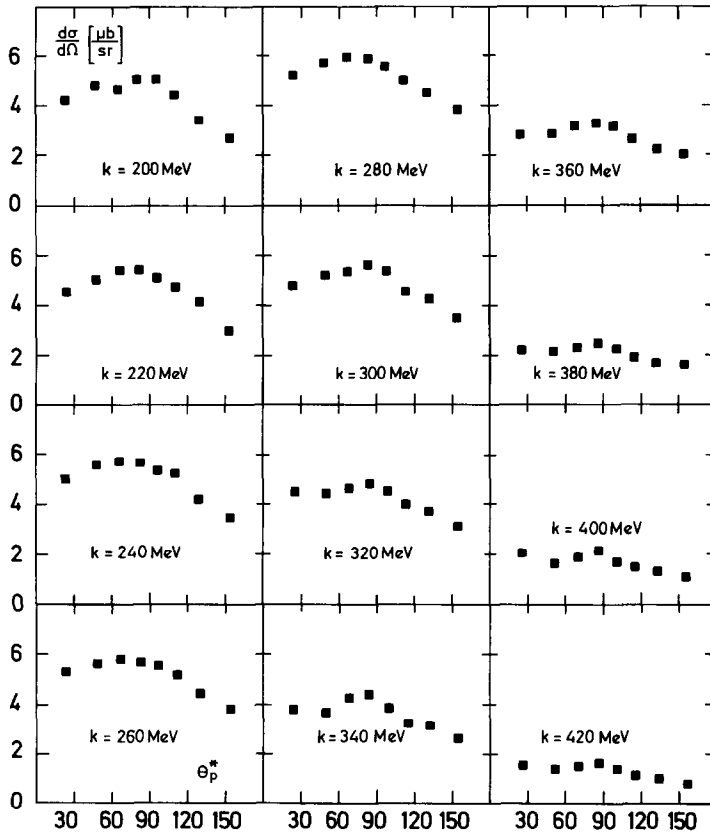

Fig. 5. Measured differential cross sections for $\gamma d \to pn$ as a function of the proton angle in the c.m.s. θ_p^*.

[†] The authors would like to thank Dr. Laget for communicating an improved version of his calculation prior to publication.
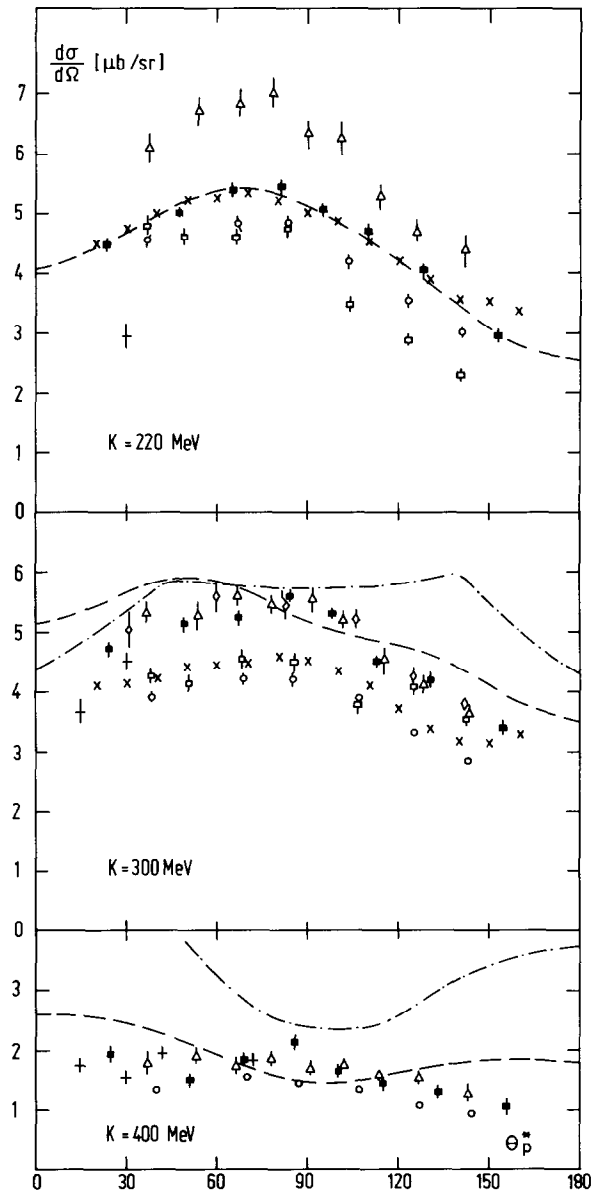
Fig. 6. Angular distribution for $\gamma d \rightarrow pn$ at $k = 220$, 300 and 400 MeV. Our data (■) are compared to the results of earlier measurements: Kose et al. [8] (□), Smith et al. [9] (▽), Buon et al. [10] (○), Anderson et al. [11] (×), Sober et al. [12] (◇), Dougan et al. [13] (△) and Baba et al. [14] (+), and to theoretical calculations by Laget [4] (dashed line) and by Anastasio and Chemtob [7] (dot–dashed line).

and Dougan *et al.* [13]) are both different in magnitude and shape. At 300 MeV our data are close to the results of Dougan *et al.* [13]) and Sober *et al.* [12]) whereas the cross sections measured by Anderson *et al.* [11]) are about 15% lower. All experiments show a maximum of the angular distribution at $\theta_p^* \approx 80°$. Laget's calculation [4]) gives a peak at $\theta_p^* \approx 50°$ while Anastasio and Chemtob [6]) predict a local minimum around 90°. At 400 MeV both calculations fail to reproduce the measured decrease of the differential cross section at backward angles.

The angular dependence of the differential cross sections was fitted by a polynomial of the form

$$\frac{d\sigma}{d\Omega} = \sum_{l=0}^{N} a_l (\cos \theta_p^*)^l$$

with photon energy dependent coefficients a_l. The order of the fit N was varied from 2 to 4. The data are already well described by the second order fit ($N = 2$). The numerical values of the coefficients for $N = 4$ are listed in table 3. The coefficient a_3 is consistent with 0 while a_4 becomes positive for $k > 300$ MeV. This behavior has also been observed by Anderson *et al.* [11]). The photon energy dependence of the coefficient a_0 (which is equivalent to the differential cross section at $\theta_p^* = 90°$) is displayed in fig. 7. This shows that, except for the Lund data [13]), most of the discrepancies between the different data sets could be removed by an adjustment of the absolute normalization.

The integration of the fit function yields the total cross sections as a function of k (also listed in table 3); it reaches a maximum of 65 μb at $k \approx 270$ MeV. In fig. 8 the results are compared to previous measurements and to theoretical predictions. As in the case of the differential cross sections the differences among the data sets can be mainly attributed to normalization problems. Laget's calculation [4]) describes our data well as far as the height of the maximum is concerned. However, the predicted peak is located at higher photon energies. The position of the peak in Arenhövel's calculation [7]) agrees better with the experiment but the absolute values are roughly 30% too high.

5. Summary and conclusions

A monochromatic photon beam has been used to measure differential cross sections for the deuteron photodisintegration process in the $\Delta(1232)$ region. The determination of both photon energy and photon flux by a bremsstrahlung tagging system and the simultaneous coverage of competing processes made an accurate measurement of the reaction possible.

Recent theoretical calculations reproduce the main features of the data. While it is obvious that considerable progress has been made towards a quantitative description of the deuteron photodisintegration the details of the measured energy and angular dependence of the differential cross sections are not yet well described.

TABLE 3

Fit parameters in $\mu b/sr$ and the total cross section $\sigma_{tot}(\gamma d \rightarrow pn)$ in μb

| k (MeV)	a_0	a_1	a_2	a_3	a_4	σ_{tot}
200	4.99 ± 0.11	1.00 ± 0.25	-2.87 ± 0.71	-0.10 ± 0.38	1.24 ± 0.81	53.7 ± 0.7
220	5.24 ± 0.08	0.95 ± 0.18	-1.49 ± 0.52	-0.08 ± 0.27	-0.48 ± 0.59	58.3 ± 0.6
240	5.53 ± 0.07	1.09 ± 0.16	-1.53 ± 0.46	-0.20 ± 0.25	-0.15 ± 0.52	62.7 ± 0.5
260	5.68 ± 0.08	1.02 ± 0.18	-1.68 ± 0.52	-0.25 ± 0.28	0.37 ± 0.60	65.2 ± 0.6
280	5.65 ± 0.08	1.23 ± 0.19	-1.41 ± 0.54	-0.61 ± 0.29	-0.05 ± 0.62	65.0 ± 0.6
300	5.37 ± 0.08	0.91 ± 0.19	-2.23 ± 0.55	-0.22 ± 0.29	0.83 ± 0.62	60.2 ± 0.6
320	4.60 ± 0.08	0.71 ± 0.19	-2.09 ± 0.54	-0.04 ± 0.29	1.27 ± 0.61	52.2 ± 0.6
340	4.16 ± 0.08	0.90 ± 0.17	-2.83 ± 0.50	-0.40 ± 0.26	1.97 ± 0.57	45.3 ± 0.5
360	3.19 ± 0.06	0.61 ± 0.14	-2.40 ± 0.41	-0.26 ± 0.22	1.73 ± 0.46	34.3 ± 0.4
380	2.39 ± 0.06	0.47 ± 0.14	-1.91 ± 0.41	-0.21 ± 0.22	1.61 ± 0.47	26.0 ± 0.4
400	1.94 ± 0.08	0.23 ± 0.18	-2.17 ± 0.52	0.24 ± 0.28	2.00 ± 0.60	20.2 ± 0.5
420	1.52 ± 0.06	0.33 ± 0.12	-1.44 ± 0.37	0.02 ± 0.19	1.22 ± 0.42	16.1 ± 0.4
440	1.21 ± 0.08	0.04 ± 0.17	-1.83 ± 0.51	0.23 ± 0.26	1.76 ± 0.58	11.9 ± 0.5

Only the statistical errors are given.
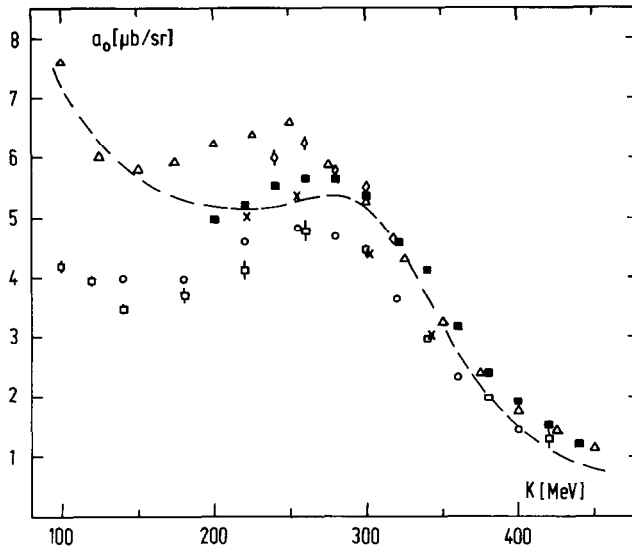
Fig. 7. Photon energy dependence of the differential cross section for $\gamma d \to pn$ at $\theta_p^* = 90°$. The cross section has been taken from the first term of a polynomial fit in $\cos \theta_p^*$.
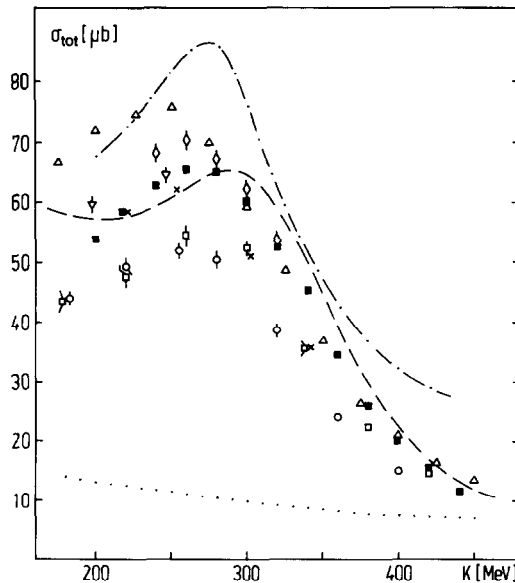

Fig. 8. Total cross section for $\gamma d \to pn$ as a function of k. Symbols for the data points as in fig. 6. The dashed curve gives Laget's full calculation [4]), the dot–dashed line represents the calculation by Arenhövel [7]). [The dotted line is Laget's calculation for the Born terms only [4]).]

Presumably, theoretical calculations will improve in the future. This will also make it necessary to increase the experimental accuracy. Both statistical and systematic uncertainties can be reduced using the high flux of tagged photons (approximately two orders of magnitude higher than the flux of our present setup) of electron accelerators with 100% duty factor.

References

1) N. Austern, Phys. Rev. **100** (1955) 1522
2) F. Zachariasen, Phys. Rev. **101** (1956) 371
3) R.R. Wilson, Phys. Rev. **104** (1956) 218
4) J.M. Laget, Nucl. Phys. **A312** (1978) 265
5) K. Ogawa, T. Kamae and K. Nakamura, Nucl. Phys. **A340** (1980) 451
6) M. Anastasio and M. Chemtob, Nucl. Phys. **A364** (1981) 219
7) H. Arenhövel, Nucl. Phys. **A374** (1982) 521c; report KPH 24/82 Mainz 1982
8) R. Kose, W. Paul, K. Stockhorst and K.H. Kissler, Z. Phys. **202** (1967) 364
9) A.M. Smith, S.J. Hall, B. Mann and D.T. Stewart, J. of Phys. **A1** (1968) 553
10) J. Buon, V. Gracco, J. Lefrancois, P. Lehmann, B. Merkel and Ph. Roy. Phys. Lett. **26B** (1968) 595
11) R.L. Anderson, R. Prepost and B.H. Wiik, Phys. Rev. Lett. **22** (1969) 651
12) D.I. Sober, D.G. Cassel, A.J. Sadoff, K.W. Chen and P.A. Crean, Phys. Rev. Lett. **22** (1969) 430
13) P. Dougan, T. Kivikas, K. Lugner, V. Ramsay and W. Stiefler, Z. Phys. **A276** (1976) 55; P. Dougan, V. Ramsay and W. Stiefler, Z. Phys. **A280** (1977) 341
14) K. Baba, I. Endo, H. Fukuma, K. Inoue, T. Kawamoto, T. Ohsugi, Y. Sumi, T. Takeshita, S. Uehara, Y. Yano and T. Maki, Phys. Rev. Lett. **48** (1982) 729
15) J. Arends, J. Eyink, H. Hartmann, A. Hegerath, B. Mecking and H. Rost, Nucl. Instr. **201** (1982) 361
16) D.F. Measday and C. Richard-Serre, Nucl. Instr. **76** (1969) 45
17) P. Benz, O. Braun, H. Butenschön, H. Finger, D. Gall, U. Idschok, C. Kiesling, G. Knies, H. Kowalski, K. Müller, B. Nellen, R. Schiffer, P. Schlamp, H.J. Schnackers, V. Schulz, P. Söding, H. Spitzer, J. Stiewe, F. Storim and J. Weigl, Nucl. Phys. **B65** (1973) 158
18) D. Menze, W. Pfeil and R. Wilcke, Phys. Data **7-1** (1977)